

Evidence for long timescale ($>10^3$ years) changes in hydrothermal activity induced by seismic events

T. HOWALD¹, M. PERSON¹, A. CAMPBELL¹, V. LUETH², A. HOFSTRA³, D. SWEETKIND³, C. W. GABLE⁴, A. BANERJEE⁵, E. LUIJENDIJK⁶, L. CROSSEY⁷, K. KARLSTROM⁷, S. KELLEY² AND F. M. PHILLIPS¹

¹New Mexico Tech, Socorro, NM, USA; ²New Mexico Bureau of Geology and Mineral Resources, Socorro, NM, USA; ³United States Geological Survey, Denver, CO, USA; ⁴Los Alamos National Laboratory, Los Alamos, NM, USA; ⁵Indian Statistical Institute, Kolkata, India; ⁶Georg-August-Universität Göttingen, Göttingen, Germany; ⁷University of New Mexico, Albuquerque, NM, USA

ABSTRACT

The pollen ^{14}C age and oxygen isotopic composition of siliceous sinter deposits from the former Beowawe geyser field reveal evidence of two hydrothermal discharge events that followed relatively low-magnitude ($<M5$) earthquakes of Holocene and late Pleistocene age along the Malpais fault zone in Whirlwind Valley, Nevada, USA. The observed 20‰ trend of decreasing $\delta^{18}\text{O}$ over about a 5000-to-7000-year period following each earthquake is consistent with a fault-controlled groundwater flow system that, following initial discharge of deep and hot groundwater, contains increasing amounts of cool meteoric water through time. Model simulations of this hydrothermal system can only match trends in the isotope data if we include a thousand-fold increase in fault permeability (from $<10^{-14} \text{ m}^2$ to $>10^{-11} \text{ m}^2$) following each earthquake. However, the timescale for onset of thermal convection implied by an overturned temperature profile in a geothermal well 300 m from the Malpais fault is much shorter: 200–1000 years. We speculate that individual segments of the Malpais fault become clogged on shorter timescales and that upward flow of groundwater subsequently follows new routes to the surface.

Key words: fault, hydrothermal, oxygen isotope, permeability, sinter

Received 2 February 2014; accepted 28 August 2014

Corresponding author: Mark Person, New Mexico Tech, Socorro, NM, USA. Email: mperson@nmt.edu
com. Tel: +1 575 835 6506. Fax: +1 575 835 6438.

Geofluids (2015) 15, 252–268

INTRODUCTION

Numerous studies have reported cm- to m-scale water-level fluctuations in wells (King *et al.* 1999; Chia *et al.* 2001; Wang *et al.* 2004; Manga *et al.* 2012), temperature changes (Dziak *et al.* 2003), increases in stream flow (Muir-Wood & King 1993), and changes in geyser periodicity (Husen *et al.* 2004) in response to seismic events. The hydrologic response to seismic waves is thought to be due to either deep-seated fracture closure/dilation (Muir-Wood & King 1993; Sibson 1996) or shallower crustal permeability changes (Rojstaczer & Wolf 1992; Broadsky *et al.* 2003; Elkhoury *et al.* 2006; Manga *et al.* 2012). Both mechanisms call upon significant permeability changes. The hydrogeologic response to seismicity can be complex (Wang *et al.* 2004) with water levels rising or falling in different locations of the stress field proximal to the

earthquake foci. Hydrologic changes have been observed to occur at great lateral distances from the earthquake epicenter (10^3 km ; Husen *et al.* 2004). In the vast majority of the above studies, the hydrologic system responded to seismic events on timescales no greater than several years (Manga *et al.* 2012). Curewitz & Karson (1994) proposed that stress changes at fault tips and fault kinematics could induce transient hydrothermal behavior on much longer timescales. Quantifiable paleohydrologic reconstructions of ore deposit formation and diagenesis have also supported hydrologic transients associated with seismicity and fault-permeability changes on timescales of 10^3 years (e.g., Garven *et al.* 2001; Appold *et al.* 2007). The objective of this study was to constrain seismicity-induced fault-permeability changes and their effects on hot spring/geyser isotopic composition over timescales of 10^3 years within the Beowawe geothermal system, Nevada. The unique

contribution of this study is a new data set of sinter-deposit ages and isotopic compositions over timescales of thousands of years.

Within Whirlwind Valley, Nevada, a large sinter terrace about 65 m high and 1600 m long (Rimstidt & Cole 1983) crops out along the Malpais fault zone, which is a high-angle normal fault with an east-northeast strike (Fig. 1A,B,D). The sinter deposits document geothermal discharge of the former Beowawe geyser field. The Malpais fault zone forms the southeastern edge of a graben that underlies Whirlwind Valley; the Muleshoe fault forms the northwestern edge (Fig. 1A). The sinter deposit formed within an area of exceptionally high heat flow at shallow depth (dashed orange lines, Fig. 2A). Zoback (1979) estimated that the sinter deposits contain 1.76×10^{10} kg of silica and that the time required to form the Beowawe sinter deposits was 210 000 years assuming a constant flow rate (Renner *et al.* 1975) and concentration of dissolved silica.

As a part of this study, we analyzed 63 sinter samples from the Beowawe geyser field for $\delta^{18}\text{O}$ (red and yellow dots in Fig. 1D). Pollen extracted from a subset of the sinter deposit samples was dated using ^{14}C (Fig. 3). The dated samples revealed isotopic depletion in fluid $\delta^{18}\text{O}$ of about 20 ‰ over 5000–7000 years that appear to be correlated with Holocene and late Pleistocene seismic activity along the Malpais fault (Fig. 3). Isotopic fractionation associated with boiling can only produce about a 2‰ shift in composition (Harris 1989) and cannot be called upon to explain the 20‰ depletion. Likewise, the effects of Quaternary climate change on the isotopic composition of precipitation in the southwestern United States are only on the order of 4‰ (Asmerom *et al.* 2010). We believe the simplest explanation for these isotopic trends is that seismicity along the Malpais fault increased fracture permeability, initiating rapid discharge of geothermal water within a single-pass hydrothermal system that, as time passed, received an increasing proportion of isotopically light meteoric water. The system gradually shut down due to mineralization and incursion of cool, dense meteoric water. One of the main goals of this study was to use thermal and isotopic modeling to test this hypothesis.

Linkages between seismicity and geyser/hot spring activity have been documented in modern geothermal systems (Wang & Manga 2010). Husen *et al.* (2004) documented temporal changes in Yellowstone geyser eruption periodicity and linked them to distant earthquakes. However, no linkages between seismicity and surface water geochemistry have been found within the Yellowstone National Park watershed (Hurwitz *et al.* 2007). Mogi *et al.* (1989) were among the first to report geothermal temperature increases in response to seismic events: a 1–2°C increase following seismic activity at Usami Hot Springs, Izu Peninsula in Japan. More recently, King *et al.* (1994) and Manga &

Rowland (2009) proposed that permeability increases following a M 5.5 earthquake led to a 1–2°C temperature decrease in Alum Rock spring, California. Diagenetic studies have also suggested episodic fluid flow events associated with seismicity along shallow fault systems. Boles & Grivetti (2000) and Boles *et al.* (2004) reported relatively high fluid-inclusion homogenization temperatures (80–125°C) at shallow depths (<300 m) along faults that crop out on the onshore region of the Santa Barbara Basin. These authors hypothesize that Pleistocene paleoseismicity increased the permeability associated with a series of faults, resulting in an episodic hydrothermal system. Paleohydrologic modeling by Appold *et al.* (2007) indicated that the combination of pressure declines with a deep overpressured reservoir and permeability changes associated with calcite cementation led to the eventual decline of hydrothermal activity over a period of about 100–1000 years. However, we are unaware of any seismicity study that has provided a high-resolution temporal record of changes in hydrothermal activity over geologic timescales.

Our study is one of the first to assess the isotopic evolution of hydrothermal fluids within a geothermal system using pollen-dated sinter deposits. We are only aware of one other study that has applied ^{14}C dating in the study of sinter deposits within the Great Basin (Lynn *et al.* 2008). They document changes in silica mineralogy (Opal-A to quartz) as a function of sinter age from the Steamboat Springs sinter deposits, NV. They analyzed terrace and distal apron samples as well as a 13.1-m-deep drill core. AMS ^{14}C pollen ages from the drill core revealed discordant ages with depth. The authors suggested that this was the result of physical mixing of older and younger sinter fragments.

STUDY AREA

Background

The Beowawe geothermal system is one of the highest temperature geothermal reservoirs in the Basin and Range physiographic province (Fig. 2A), with a temperature of about 220°C at 3 km depth (Olmsted & Rush 1987). The system is liquid dominated; boiling is localized at very shallow depths. The most recent volcanism in the area occurred during the middle Miocene and is not considered a feasible heat source. The low helium R/R_A value of 0.46 reported by Welhan *et al.* (1988) is also indicative of an amagmatic system. The Beowawe geothermal system is located within the Battle Mountain high heat flow, which has a background heat flow of about 110 mW m⁻² (Smith 1983). This is believed to be partially due to a thinned crust (19–23 km; Heimgartner *et al.* 2006). Shallow temperature-gradient measurements indicate heat flow <2000 mW m⁻² (Olmsted & Rush 1987). The large shallow heat flow is thought to be associated with deep-seated

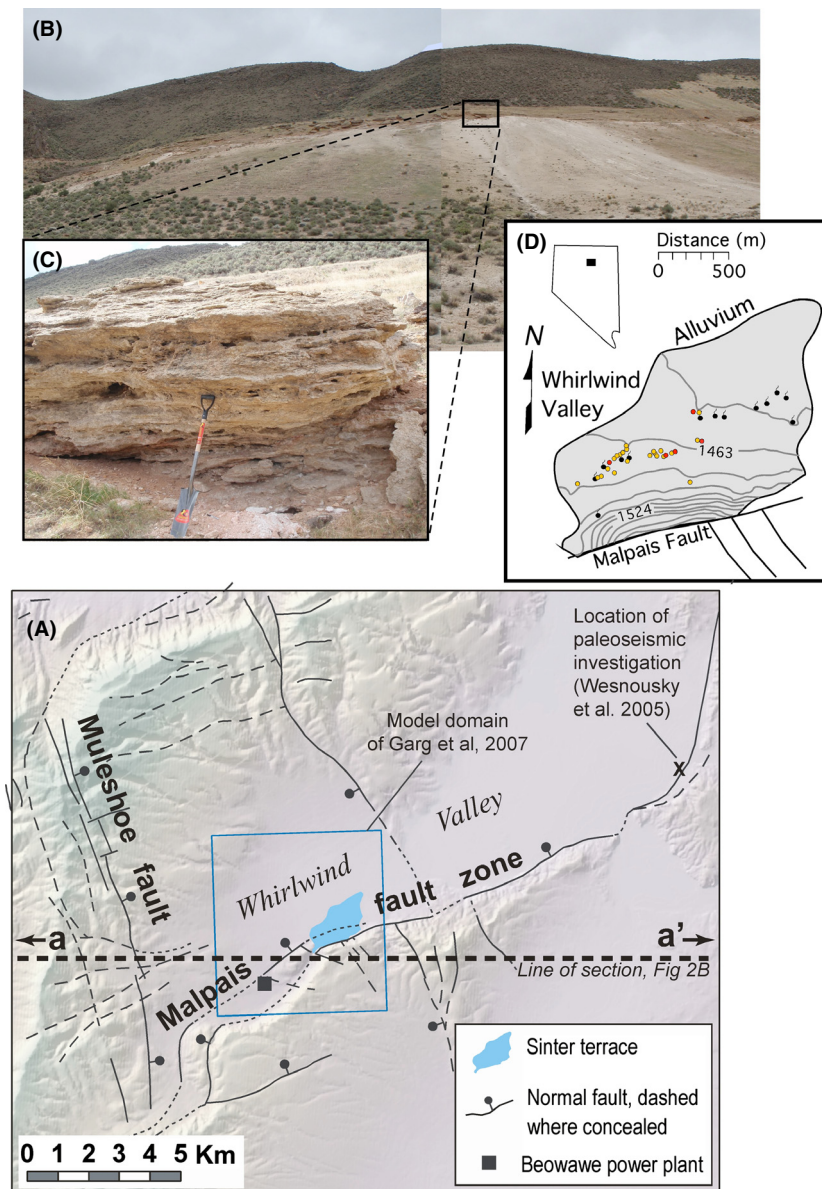


Fig. 1. (A) Structural map showing location of Beowawe sinter deposits, paleoseismic investigation of Wesnousky *et al.* (2005) along the Malpais fault zone, the Beowawe power plant (black square). (B) Photograph mosaic of Beowawe sinter deposits, Whirlwind Valley, Nevada. The photograph was taken looking southeast. (C) Outcrop scale photograph of sinter deposits. (D) Sinter topographic map with locations of historic and paleo-hot springs (black circles, as well as locations of sinter samples (red and yellow circles). Multiple samples were collected at locations with yellow dots.

and permeable normal faults that allow hot fluids to be brought up to the surface quickly. Geothermal waters discharge at a high rate (18 kg s^{-1}) along the Malpais fault zone, where volumetrically significant sinter deposits have accumulated (Zoback 1979).

The permeability of the Malpais fault zone has been estimated by several prior studies. Faulder *et al.* (1997) reported well pressure tests that were used to estimate the Malpais fault zone permeability. They reported that fault zone conductance to be between about 6×10^{-11} and $1.2 \times 10^{-10} \text{ m}^3$. Person *et al.* (2008) developed a paleo-hydrothermal model of gold mineralization to assess the plumbing of the Miocene age Mule Canyon gold deposits in Whirlwind Valley. They assigned a vertical permeability of 10^{-11} m^2 to the Muleshoe and Malpais faults in their

basin-scale, cross-sectional hydrothermal model of Whirlwind Valley. Garg *et al.* (2007) developed a three-dimensional, single-phase, fault-scale (about $3 \text{ km} \times 3 \text{ km} \times 3.5 \text{ km}$; blue box in Fig. 1A) hydrothermal and solute transport model of the Malpais fault zone to reproduce direct-current resistivity, magnetotelluric, and well temperature surveys. Two of the six wells studied by these authors, those closest to the Malpais fault zone (Balz-1, 85-15; see Fig. 4B–C), displayed pronounced temperature overturns with depth consistent with a transient geothermal flow system (Ziagos & Blackwell 1986). To match observed temperature data (Fig. 4A–D), Garg *et al.* (2007) assigned a permeability of $2 \times 10^{-13} \text{ m}^2$ to a 1.2-km-long and 3-km-deep section of the Malpais fault zone, while the remaining segments of the Malpais fault were

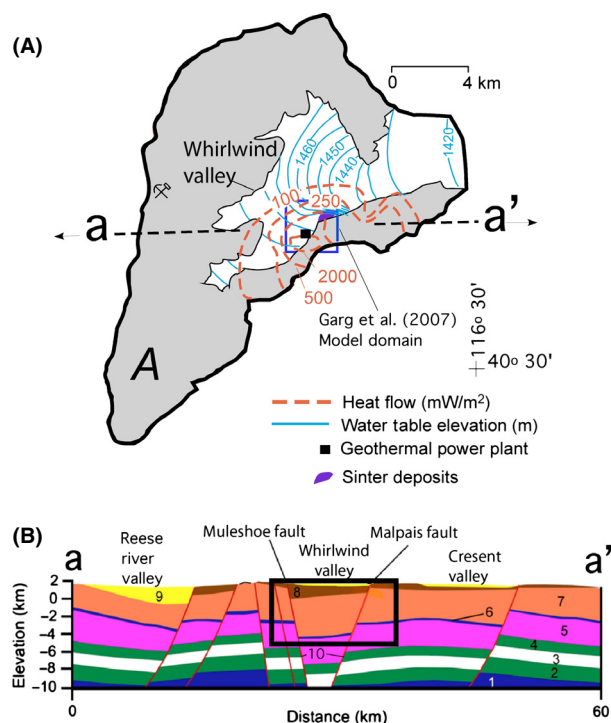


Fig. 2. (A) Heat flow (orange dashed contour lines; in mW m^{-2}) and water-table elevation (solid light blue lines; m) contour map across Whirlwind Valley, NV. Location of regional hydrothermal model cross-section is depicted by a-a'. Dark blue box indicates the location of the Beowawe sinter terrace shown in Fig. 1B. Heat-flow and water-table contour maps from Olmsted & Rush (1987) and Faulder *et al.* (1997). (B) Hydrogeologic cross-section across Reese, Whirlwind, and Crescent Valleys. The inset (solid black rectangle) denotes the portion of the hydrothermal model domain presented Fig. 7A–F. Permeability data for the different numbered units in Fig. 2B are presented in Table 6.

assigned 10^{-15} m^2 . The model included a specified fluid flux of 20 kg s^{-1} along the base of the Malpais fault (at about 3 km depth) to match observed geothermal discharge and was run for 25 000 years, sufficiently long to approach quasi-steady-state thermal conditions. While the Garg *et al.* (2007) model was able to simulate temperatures that were a good match to four of the six wells, the observed thermal overturns (Fig. 4B–C) in the wells closest to the Malpais fault zone could not be reproduced. This may be because the model represents late-time (25 000 years), quasi, steady-state conditions, and the overturned temperature profiles are likely the result of a short-term transient fluid pulse (Ziagos & Blackwell 1986).

History of geothermal development at beowawe

The Beowawe geothermal system has been under scientific investigation since 1934. Detailed reports on the geology, structure, and hypothesized hydrothermal fluid flow

pathways can be found in Zoback (1979) and Struhsacker (1980). Both of these papers provide detailed geologic maps of the area, lithologic descriptions of the rock units, cross-sections derived from geothermal wells, and summaries of the geologic history.

The Beowawe geothermal system was once the second largest site in the United States for active geyser, fumarole, and hot spring activity, second only to Yellowstone National Park. Today, these geothermal discharges have subsided, and Beowawe is host to only a large sinter terrace and a few fumaroles (Fig. 1B–C). This change is likely due to geothermal fluid production, which began in 1985 with a 16.7-MW dual-flash power plant (square, Fig. 1A).

White (1998) published a detailed report on the Beowawe geothermal system before, during, and after geothermal drilling and development. The report includes pictures of the formerly active geysers and springs, geologic and hydrologic maps of the geysers and Whirlwind Valley area, and a table summarizing water geochemistry from previous studies of the Beowawe geothermal system. This report, along with the article published by Nolan & Anderson (1934), provides a detailed characterization of the Beowawe geothermal system before geothermal development.

Conceptual model of transient hydrothermal flow within the beowawe geothermal system

We propose that the isotopic trends presented in Fig. 3 are the result of a transient, single-pass hydrothermal system of the type described by Lowell (1991) (Fig. 5). We hypothesize that within the discharge area (Malpais fault, Fig. 1A, 2B), initially hot, isotopically enriched fluids discharged at the surface following a seismic event. Discharge temperature and isotopic composition peaked shortly after the onset of flow. The brief lag time is required for deep reservoir fluids to make their way up to the surface. In the recharge area, in response to temporarily enhanced fault permeability, we hypothesize that isotopically depleted meteoric water flowed downward along fault conduits (here the Muleshoe Fault Zone, Fig. 1A, 2B), moved laterally through the karst reservoir (thin dark blue unit in Fig. 2B) picking up heat, and then discharged at the surface along the Malpais fault. The ^{18}O of the meteoric water increased along the flow path due to mixing with geothermal reservoir fluids (karst aquifer, see unit 6, Fig. 2B) and fluid–rock isotope exchange. However, as the flow system evolved over time, the discharging fluids trended toward a meteoric composition. Lowell *et al.* (1993) showed that discharge temperature is controlled by the product of fault zone width and permeability or conductance (kb), and showed that hot spring temperature peaks at intermediate values of fault conductance. This is because at the highest flow rates (or widest fault zones),

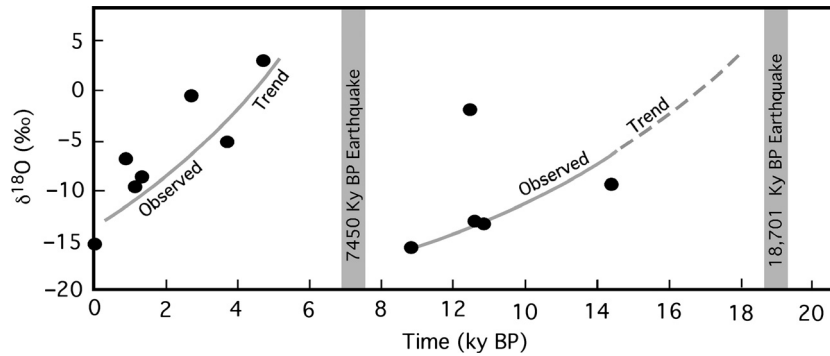


Fig. 3. Reconstructed temporal evolution of fluid compositions based upon calculated $\delta^{18}\text{O}_{\text{H}_2\text{O}}$ (at 93°C) in equilibrium with sinter and radiocarbon dates on pollen in sinter (circles). The best fit dashed gray lines drawn through the sample points show that $\delta^{18}\text{O}_{\text{H}_2\text{O}}$ progressively decreased during two distinct episodes of fluid flow through the Beowawe geothermal system. Timing of earthquakes reported by Wesnousky *et al.* (2005) suggests each episode of fluid flow was triggered by seismicity. Initially, hot fluids are in isotopic equilibrium with the carbonate reservoir rocks at 5-km-depth discharge. Introduction of isotopically depleted meteoric water through time results in the progressive decrease in isotopic composition of discharging fluids along the Malpais fault. Sample point on the origin of the Y-axis (-15‰) is the present-day average $\delta^{18}\text{O}_{\text{H}_2\text{O}}$ value at Beowawe for precipitation (John *et al.* 2003).

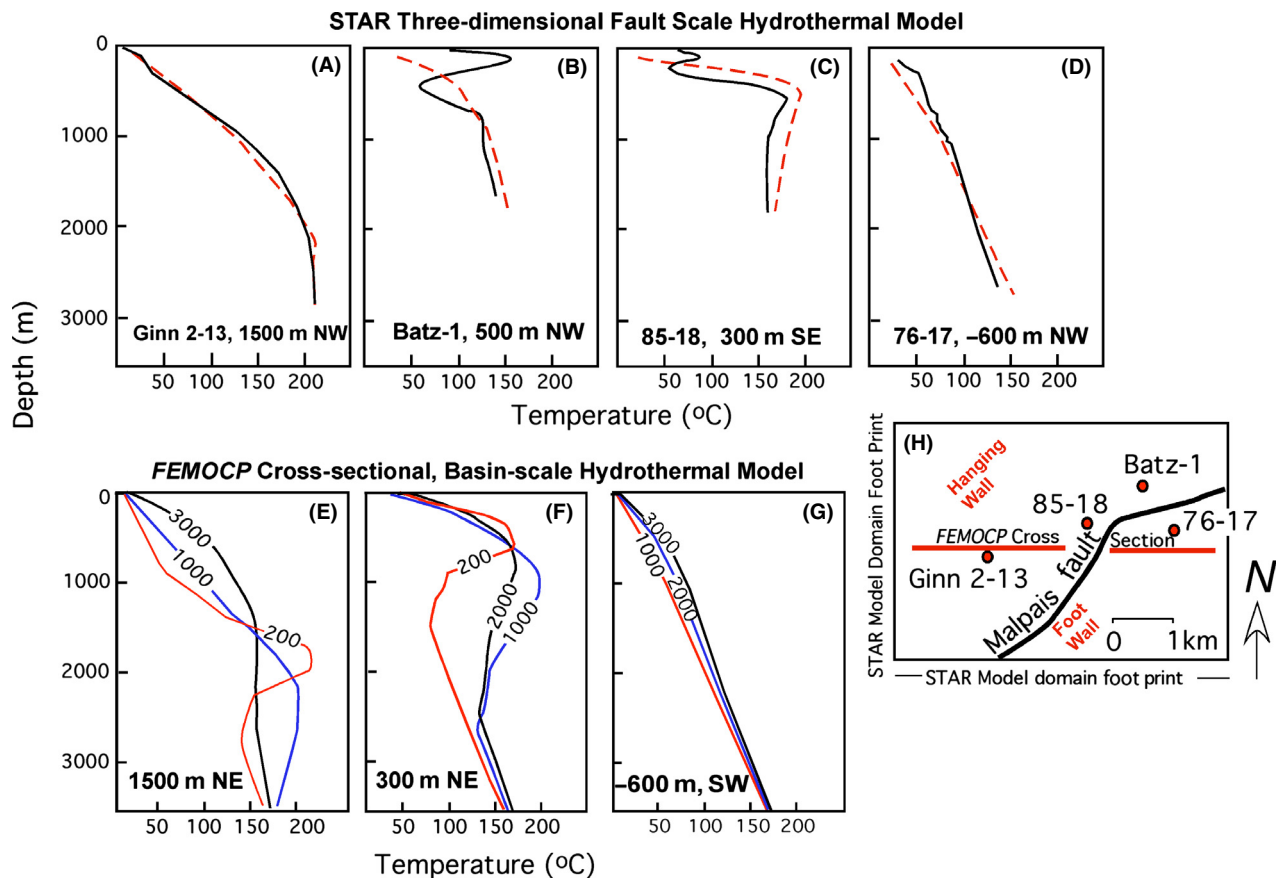


Fig. 4. (A–D) Observed (solid black lines) and computed (red dashed lines) temperature profiles from three-dimensional, fault-scale, hydrothermal STAR model of Malpais fault Zone. Well distances from Malpais fault and well name are listed in the lower left-hand corner of each plot. All computed temperatures are after 25 000 years (after Garg *et al.* 2007). (E–G) Time-dependent evolution of computed temperature profiles extracted from FEMOCP cross-sectional, basin-scale hydrothermal model at different distances from the Malpais fault zone using 'best fit' Malpais zone fault permeability of 10^{-12} m^2 . Location of wells and the STAR model footprint are shown in Fig. 2H along with the location of the FEMOCP cross-sectional transect.

the recharge increases to the point that it has a net cooling effect on the hydrothermal system. For lower permeability conditions, heat conduction dominates. In the conceptual

model presented in Fig. 5, the groundwater flow is driven by the water-table topographic gradient. It is likely that density effects also contribute significantly to driving fluid

flow up the Malpais fault zone at Beowawe (Person *et al.* 2008).

Another independent line of evidence that argues for transient hydrothermal fluid flow within the Beowawe geothermal system comes from the analysis of bore-hole temperature profiles. Present-day bore-hole temperature profiles proximal to the Malpais fault zone show temperature overturns (solid black lines in Fig. 4B–C). Ziagos & Blackwell (1986) showed that such temperature overturns result in transient lateral flow of geothermal fluids (Fig. 6). These authors developed analytical and numerical solutions for transient temperature profiles associated with lateral fluid flow into a shallow aquifer. They considered the consequences of hydrothermal fluids moving up a fault zone and then laterally into a shallow aquifer (Fig. 6A), and showed that after the onset of lateral flow, temperature profiles in wells displayed a distinctive thermal overturn that decreased with increasing distance from the fault zone (Fig. 6B). At late time, however, the overturns dissipate due to downward heat conduction (Fig. 6C). Ziagos & Blackwell (1986) also presented numerical results using the fast Fourier transform method to investigate time-dependent changes in the enthalpy of the discharging fluids. In this scenario, high enthalpy fluids were input for 1000 years, followed by lower enthalpy fluid input. Fluid temperatures within the water-table aquifer rose quickly at first, followed by a more gradual temperature increase. Once cool fluids were introduced after 1000 years, the opposite pattern developed: rapid cooling followed by a more gradual temperature decline. We argue below that the post-1000-year temperature declines shown in Fig. 6D are analogs to time-dependent changes in isotopic composition of geothermal fluids within the Beowawe geothermal system (Fig. 3). One issue we must address in this study is that the onset of convection we estimate from the temperature profile data in Fig. 4B–C is considerably shorter than the duration of flow revealed by the isotopic data in Fig. 3.

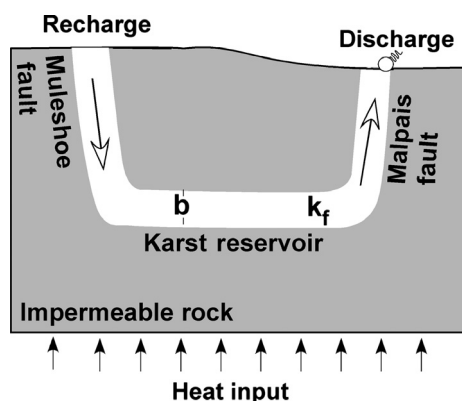


Fig. 5. Conceptual diagram depicting single-pass model of a hydrothermal system having a conduit width of 'b' and a fault zone permeability of k_f . In this diagram, circulation is driven by a hydraulic head gradient between the upland and lowlands (after Lowell 1991).

The onset of convection appears to be correlated with Holocene and late Pleistocene seismic events along the Malpais fault zone (see X, Fig. 1A), which hosts the sinter deposits (Fig. 3; Wesnousky *et al.* 2005). The age of each paleoseismic event along the Malpais fault was estimated using ^{14}C dates on carbonaceous material in soil layers that are truncated by the fault (Wesnousky *et al.* 2005). The small size (<0.5 m) of the offsets between colluvium layers along the fault (Wesnousky *et al.* 2005) suggests these were low-energy earthquakes ($<M5$) (Friedrich *et al.* 2004). We hypothesize that flow commences following permeability increases along subvertical faults following seismicity (Wang & Manga 2010; Fig. 5). Hot, silica-rich fluids within a deep (approximately 5 km depth) carbonate geothermal reservoir move up the Malpais fault and discharge at the surface (Fig. 2B). Progressive silica mineralization and influx of cool meteoric fluids along the fault zone eventually shut the convective flow system down or at least reduce rates of sinter formation (Lowell *et al.* 1993). To test the above hypotheses, we constructed a series of geologically referenced hydrothermal models that include fluid–rock oxygen-isotope transport and exchange (Bowman *et al.* 1994) within the Beowawe geothermal system. We systematically vary the permeability of the fault zones to constrain the magnitude of permeability changes following a seismic event in a fashion that is consistent with the sinter-deposit data. We address the following questions: (i) What fault permeability is consistent with present-day conditions within the Beowawe geothermal system? (ii) How large of a permeability increase is required to enhance hydrothermal activity within Beowawe geothermal system? (iii) Does a single-pass geothermal system with progressive influx of meteoric water produce a trend of decrease isotopic composition consistent with the sinter data we collected? (iv) Over what timescales does this occur? (v) Assuming that the flow system shuts down at late time, how long does it take the isotopic fluid composition in the deep carbonate reservoir to recover?

METHODS

Sample preparation

We collected 63 sinter samples between 2009 and 2012 along the Beowawe siliceous sinter terrace within Whirlwind Valley (Fig. 1D) to establish the periodicity of hydrothermal activity in the Beowawe geothermal field. Almost all of the samples were collected at the surface and along a single road cut. All of the sinter samples were analyzed for mineralogy, crystallinity, and oxygen-isotope composition. Pollen and charcoal extracted from 11 sinter samples were dated using radiocarbon methods (Table 1).

To separate organic matter from mineral grains, the sinter was treated with a 50% hydrogen peroxide solution to

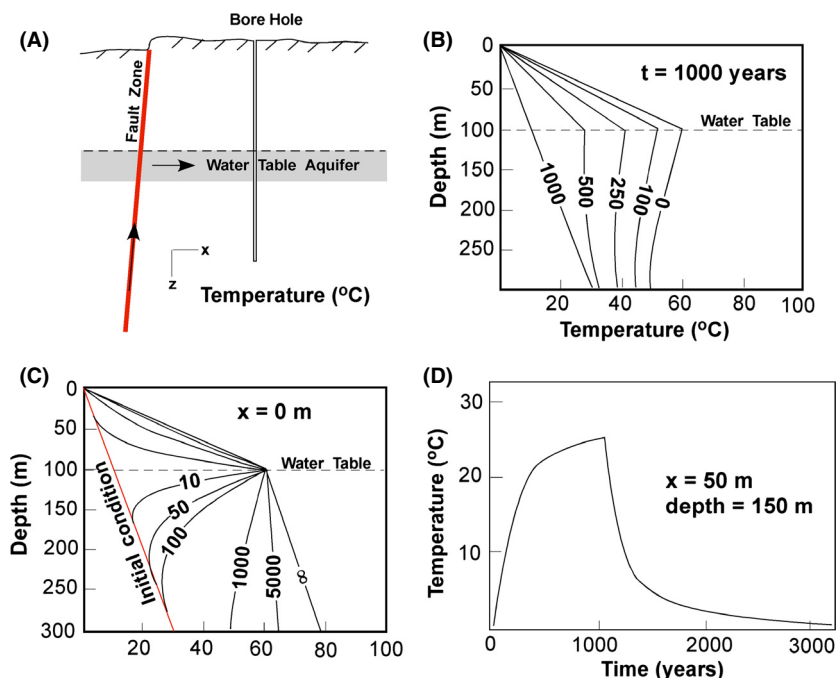


Fig. 6. (A) Schematic diagram depicting conceptual model for time-dependent analytical solution of thermal transients presented by Ziagos & Blackwell (1986). The Laplace transform analytical solution was developed to represent temperature changes in wells resulting from lateral outflow of hot geothermal fluids that move up a fault zone and out into a shallow water-table aquifer. (B) Changes in temperature along a well bore after 1000 years of lateral flow rate at 1 m year^{-1} . The initial geothermal gradient was $100^\circ\text{C km}^{-1}$. Profile labels are the distance of the well bores from the fault zone in meters. (C) Temperature changes through time at a well bore located at the fault zone ($x = 0 \text{ m}$). Profile labels denote time since the onset of flow. Note that at early times, temperature overturns occur. At late time, the temperature inversions are erased by downward heat conduction. (D) Fast Fourier transform solution for time-dependent changes in temperature 50 m from the fault zone at a depth of 150 m below the water table. Changes in temperature are due to time-dependent changes in the enthalpy of the fluid entering the shallow water-table aquifer. A step function is used to represent inflow of initially hot water for 1000 years followed by cooler water inflow (after Ziagos & Blackwell 1986).

remove any organic material trapped in pores and outer surfaces. The samples were rinsed with water, oven dried, and crushed. The crushed material was treated in 10% HCl to remove carbonates and then in 50% HF to remove silicates. The sinter material was then washed three times in 10% HCl and then in water. The remaining material was separated using a 150-micron sieve. The organic matter larger than 150 μm was collected in a centrifuge tube. The material $<150 \mu\text{m}$ was sieved at 6 μm , and particle sizes between $6 \mu\text{m} < X < 150 \mu\text{m}$ were collected. Multiple gravity separations were also performed using sodium polytungstate (density 2.0 g ml^{-1}) to remove remaining insoluble minerals. Plant fragments that floated at 2.0 g ml^{-1} were then sieved using a 6-micron filter and rinsed with water. The float material was loaded into a combustion tube. The radiocarbon activity of the pollen/charcoal samples was then analyzed at Rafter Radiocarbon Laboratory in New Zealand using an accelerator mass spectrometry.

Sinter mineralogy analysis

The mineralogy and crystallinity of the sinter samples was determined using X-ray diffraction (XRD). Samples were

dried in an oven at 60°C to remove any water present and then hand ground to pass through a $150\text{-}\mu\text{m}$ mesh sieve. The composition of the sinter deposits was determined using a PanAnalytical XPert Pro diffractometer and methods outlined in Herdianita *et al.* (2000). The sinter samples were analyzed using $\text{CuK}\alpha$ radiation for 15 min each over a range of 10° to $40^\circ 2\theta$ and a step size of 0.0170° . XRD patterns were interpreted using PANALYTICAL X'PERT HIGHSCORE PLUS software to determine the crystallinity (order/disorder) of the opaline phase of the sinters. Crystallinity can be measured as the full-width half-maximum (FWHM) by manually fitting a profile and baseline to the diffraction pattern and then measuring the width of the band at half intensity (Herdianita *et al.* 2000). The sinter terrace at the Beowawe geothermal system consists primarily of Opal-A, Opal-A/CT, Opal-CT/A, or Opal-CT and indicates that geothermal fluids were saturated with respect to amorphous silica. Rimstidt & Cole (1983) argue that the amorphous silica comprising the sinter deposits at Beowawe precipitated at temperatures of $88\text{--}98^\circ\text{C}$. Measured temperatures of geothermal fluids in the 'Frying Pan' geyser and another small geyser were about 95 and 98°C , respectively, prior to exploitation (Nolan & Anderson 1934; Mariner *et al.* 1983).

Table 1 Oxygen isotopic composition and radiocarbon dates of pollen taken from sinter deposits.

Sample Number	Age (years)	Con. Int. (year)	$\delta^{13}\text{C}$ (‰)	Primary Minerals	Latitude	Longitude	$\delta^{18}\text{O}_{\text{sinter}}$	$\delta^{18}\text{O}_{\text{fluid @ } 90^\circ\text{C}}$
B-1c	10454	±40	-25.3	Opal, Qtz, Kaolinite	N40°33'44.5"	W116°35'25.9"	20.10	-2.20
B-8	4706	±25	-20	Opal	N40°33'41.4"	W116°35'29.4"	24.93	2.63
B-14a	893	±25	-23.6	Opal, Plagioclase	N40°33'36.4"	W116°35'40.8"	15.1	-7.2
B-15	2684	±25	-24.5	Opal	N40°33'38.0"	W116°35'34.2"	21.4	-0.9
B-19c	1137	±20	-22.3	Opal, Qtz	N40°33'43.1"	W116°35'10.7"	12.5	-9.8
B-3	8797	±60	-29.2	Opal, Qtz, Kaolinite	N40°33'42.8"	W116°35'26.9"	6.93	-15.37
B-5	14375	±70	-29.6	Opal	N40°33'38.7"	W116°35'29.1"	12.56	-9.74
B-6 btm	10774	±50	-29.1	Opal	N40°33'40.50"	W116°35'33"	8.77	-13.54
B-7	10580	±50	-29.3	Opal	N40°33'41.5"	W116°35'29.3"	8.90	-13.41
B-11 wht	3693	±30	-26.3	Calcite, Cristobalite, Sanidine	N40°33'30.29"	W116°35'21"	16.90	-5.40
B-10b	1322	±40	-26.1	Opal	N40°33'38.7"	W116°35'29.1"	13.4	-8.9

Sinter oxygen-18 analysis

Stable-isotope analysis of oxygen from the opal samples was performed using New Mexico Tech's fluorination line following Borthwick & Harmon (1982) and Baertschi & Silverman (1951). Powdered samples were reacted with dilute HCl to remove any carbonate, then rinsed with distilled water, and dried in an oven at 60°C for 12 h. Samples were prefluorinated with ClF_3 in nickel reaction vessels for 10 min at room temperature to ensure that all remaining water was removed from the samples and reaction chambers, then reacted with ClF_3 at 500°C for 8 h. The liberated oxygen gas was converted to CO_2 with a carbon electrode. The CO_2 gas was analyzed via dual inlet on the Delta XP IRMS spectrometer for $\delta^{18}\text{O}$ using an OZ-Tech CO_2 gas standard. Samples that produced yields below 60% were not used for interpretation. Samples that produced yield values between 60 and 80% were analyzed two or three times and then averaged with a reproducibility of ± 0.8 . The isotopic composition of water ($\delta^{18}\text{O}_{\text{H}_2\text{O}}$) was calculated from that of sinter ($\delta^{18}\text{O}_{\text{sinter}}$) at 93°C using the equilibrium fractionation factor of Kita *et al.* (1985) ($1000 \ln \alpha_{\text{(amorphous SiO}_2\text{-H}_2\text{O)}} = 21.9$). The temperature selected is within the limits of the fractionation equation and the reported range of fluid temperatures in the geyser field where sinter was deposited.

Single-phase, single-pass hydrothermal model description

To interpret the stable-isotope history of the sinter deposit and the present-day temperature trends, we constructed a relatively simple, cross-sectional, single-phase hydrothermal model of the Beowawe geothermal system. In this model, permeability is instantaneously increased along the Muleshoe and Malpais fault zones (unit 10, Fig. 2B) to create a single-pass hydrothermal system. Manga *et al.* (2012) argued that this type of permeability change can be caused by removal of small particles that block fault apertures. In our model, the faults are connected to permeable geothermal reservoir at depth, a karst

subunit within the Great Basin Paleozoic aquifer system (unit 6, Fig. 2B). Based upon geophysical, geologic, and drilling information, the source reservoir for the geothermal fluids is interpreted to be Paleozoic carbonate 3–5 km below the surface (Watt *et al.* 2007). This interpretation is confirmed by the $\delta^{13}\text{C}$ compositions of dissolved inorganic carbon in Beowawe geothermal fluids (-2 to 1‰), which is typical of Paleozoic marine limestones (Day 1987). The isotopic composition of water and dissolved inorganic carbon at Beowawe reported by Day (1987) was further discussed by John *et al.* (2003, p. 460–461). The δD of the water (-115‰) is about 10‰ less than modern meteoric water in the area. Such values are common in active hot springs across the Basin and Range province, USA, and have been interpreted to reflect the involvement of Pleistocene meteoric water in these systems (Smith *et al.* 2002). Day (1987) attributed the high $\delta^{13}\text{C}$ values (-2 to 1‰) to dissolution of Paleozoic limestone (-2.5 to 3‰) situated at deep levels (approximately 3000 m) below siliciclastic rocks of the Roberts Mountains thrust. Given the high reservoir temperature (approximately 220°C), the small $\delta^{18}\text{O}$ shift from the meteoric water line ($<3\text{‰}$) requires large water:rock ratios (approximately 10; John *et al.* 2003) and a permeable fault and/or karst-controlled flow system. Early Paleozoic marine carbonate rocks in Nevada have $\delta^{18}\text{O}$ values that range from approximately 20 to 30‰ (Hofstra & Cline 2000). Over time, fluids in a high-temperature reservoir will equilibrate with the surrounding rocks and shift to higher $\delta^{18}\text{O}_{\text{H}_2\text{O}}$ values. The aforementioned range of carbonate-rock compositions and the fractionation equation of Kim & O'Neil (1997), ($1000 \ln \alpha_{\text{calcite-H}_2\text{O}} = 4.14 @ 220^\circ\text{C}$) show that an equilibrated reservoir fluid will have $\delta^{18}\text{O}_{\text{H}_2\text{O}}$ values between 16 and 26‰ , comparable to the higher $\delta^{18}\text{O}_{\text{H}_2\text{O}}$ values from the sinter deposits (Fig. 3). The lowest $\delta^{18}\text{O}_{\text{H}_2\text{O}}$ values in Fig. 3 appear to require a component of meteoric water.

Our paleohydrologic model includes calculations of groundwater flow rates, temperatures, and fluid–rock isotopic interactions/transport. The Beowawe hydrogeologic

cross-section was constructed along an east–west transect across the southern part of Whirlwind Valley (a–a', Fig. 1A, 2A–B). It extends to the adjacent Reese River and Crescent Valleys, which enables us to consider the possibility of interbasin transfers of groundwater. These were found to be negligible (Person *et al.* 2008). Model results presented here are focused on Whirlwind Valley, which hosts the Beowawe geyser field.

The governing transport equations are presented in Table 2. Like Garg *et al.* (2007), our model is not capable of representing boiling conditions. In addition, mineral dissolution–precipitation reactions and their effects on fault permeability are not considered (e.g., Lowell *et al.* 1993). The detailed stratigraphy along this section was generalized into a limited number of hydrogeologic units comprised of stratigraphic units inferred to have similar hydrologic properties. Geologic structure was similarly generalized such that the only structures portrayed on the sections are either those that have sufficient offset to juxtapose different hydrogeologic units or structures that were explicitly included as part of the flow scenario being tested. In certain cases, structures that were subparallel to the section were omitted or generalized as a fault more nearly perpendicular to the section trace. Although based on surface and subsurface geologic and geophysical data, the hydrogeologic cross-sections are intended to represent generalized scenarios that contain the salient geologic features needed to test a flow hypothesis; they are not intended to be literal representations of all that is known concerning the subsurface geology.

The hydrothermal model used in this study considered the effects of both topography-driven and density-driven single-phase groundwater flow (Raffensperger & Garven 1995). The fluid flow (eq. 1, Table 2) and heat-transport equations (eq. 2, Table 2) were coupled using temperature- and pressure-dependent density and viscosity relations from Batzle & Wang (1992). In this study, the transients are driven mainly by permeability changes. We represented advective–dispersive isotope transport and fluid–rock isotope exchange (eqs 4–5, Table 2) using a kinetic-based approach described by Bowman *et al.* (1994). We assumed that each lithologic unit was composed of seven different minerals, each having its own isotopic fluid–rock exchange parameters and initial isotopic composition (Tables 3–4). Temperature-dependent equilibrium isotope fractionation factors, pre-exponential factor (A_0), and the activation energy (E_a) for each of the m^{th} mineral phases were taken from experimental data reported by Zhang *et al.* (1994), Zheng (1999), and Sheppard & Gilg (1996).

In the groundwater-flow equation, we specified a constant value ($\Psi = 0$) stream-function boundary along the sides and base of the domain consistent with a no-flux boundary condition. We specified a flux ($d\Psi/dz$) boundary

Table 2 Governing transport equations.

Stream Functions	
$\nabla_x \cdot \left[\frac{k}{ k } \nabla_x \psi \right] = -\frac{\partial \rho_f}{\partial x}$	(1)
Cauchy-Riemann Equations	
$q_x = \frac{\partial \psi}{\partial z} \quad q_z = -\frac{\partial \psi}{\partial x}$	(2)
Heat Transport	
$\nabla_x \cdot [\lambda \nabla_x T] - \bar{q} \rho_f c_f \nabla_x T = [\phi \rho_f c_f + (1 - \phi) \rho_s c_s] \frac{\partial T}{\partial t}$	(3)
Fluid-Rock Isotope Transport	
$\nabla_x \cdot [D \nabla_x R_f] - \frac{\bar{q}}{\phi} \nabla_x R_f = \frac{\partial R_f}{\partial t} + \frac{\partial R_{rk}}{\partial t} \frac{X_{rk}}{X_f}$	(4)
Kinetic Fluid-Rock Isotope Exchange	
$\frac{dR_{rk}}{dt} = \bar{A}_{rk} [\alpha_{rk} R_f - R_{rk}]$	(5a)
$\alpha_{rk} = \sum_{m=1}^M f_m \alpha_m$	(5b)
$R_{rk} = \sum_{m=1}^M A_0^m \exp \left[-\frac{E_a^m}{Rt} \right]$	(5c)
Thermal Conduction-Dispersion Tensor	
$\lambda_{xx} = \rho_f c_f \alpha_L \frac{q_x^2}{ q } + \rho_f c_f \alpha_T \frac{q_z^2}{ q } + \lambda_f \phi + (1 - \phi) \lambda_s$	(6)
$\lambda_{zz} = \rho_f c_f \frac{q_x^2}{ q } \alpha_T + \rho_f c_f \frac{q_z^2}{ q } \alpha_L + \lambda_f \phi + (1 - \phi) \lambda_s$	
$\lambda_{zx} = \lambda_{xz} = (\alpha_L - \alpha_T) \frac{q_x q_z}{ q }$	
Solute Diffusion-Dispersion Tensor	
$D_{xx} = \alpha_L \frac{v_x^2}{ v } + \alpha_T \frac{v_z^2}{ v } + D_d$	(7)
$D_{zz} = \alpha_T \frac{v_x^2}{ v } + \alpha_L \frac{v_z^2}{ v } + D_d$	
$D_{zx} = D_{xz} = (\alpha_L - \alpha_T) \frac{v_x v_z}{ v }$	

k is hydraulic conductivity tensor; g is gravity; ∇_x is the gradient operator; h is hydraulic head; ρ_r is the relative density ($\rho_r = (\rho_f - \rho_o)/\rho_o$); ρ_o is the reference fluid density; ρ_f is fluid density at elevated temperature and pressure; x and z are the spatial coordinates; Ψ is the stream function; $|k|$ is the determinant of the hydraulic conductivity tensor; T is temperature; q_x and q_z are the components of Darcy flux in x and z directions; c_f is the specific heat capacity of the fluid; c_s is the specific heat capacity of the solid; ϕ is porosity; λ_{xx} , λ_{zx} , λ_{xz} , λ_{zz} are the components of the thermal conductivity–dispersion tensor of the porous medium; D_{xx} , D_{zx} , D_{xz} , D_{zz} are the components of dispersion–diffusion; $|v|$ is the magnitude of velocity; D_d is the molecular diffusion coefficient for porous media; q_x and q_z are the components of Darcy flux in the x - and z -directions, respectively; α_L and α_T are the longitudinal and transverse dispersivities, respectively; R_f is the fluid isotopic ratio; R_{rk} is the bulk rock isotopic ratio (averaged over all mineral phases present); t is time; X_{rk} is the fractional abundance of oxygen in the bulk rock phase; X_f is the fractional abundance of oxygen in water; \bar{A} is the bulk rock reactive surface area; r_{rk} is the bulk rock reaction rate for fluid–rock isotope exchange; α_{rk} is the bulk fluid–rock equilibrium isotope-exchange factor averaged over all oxygen-bearing mineral phases; M is the total number of oxygen-bearing mineral phases for a given rock; A_0^m is the pre-exponential factor of the m^{th} mineral phase; E_a^m is the activation energy for the exchange reaction; R is the ideal gas constant. Note that temperature is in Kelvin for isotope-exchange reactions.

condition across the top of the model domain with the magnitude of the flux being proportional to the lateral water-table gradient (Fogg & Senger 1985). For heat transfer, a specified temperature of 10°C was imposed along the top boundary except at the Malpais fault zone, where groundwater discharges. Here, a no-flux boundary

Table 3 Mineral isotopic parameters.

X_m	c_m	d_m	e_m	f_m	ρ_m	A_o	E_a	Initial $\delta^{18}\text{O}$ Composition	Mineral
0.5325	0.0	3.306	0.0	-2.71	2650	3.46E-05	11	10	Quartz*
0.13	-0.388	5.538	-11.35	3.132	2850	4.50E-08	6.5	26	Dolomite†
0.48	-0.891	8.557	-18.11	8.27	2710	4.50E-08	6.5	26	Calcite†
0.1343	0.0	2.76	0.0	-6.75	2600	0.0000047	9.5	16	Kaolinite‡
0.2747	0.0	3.904	-5.47	1.86	4500	0.0475	13.4	20	Barite
0.4180	0.0	4.12	-7.5	2.24	2700	1.39E-07	26.2	20	Anorthite

A_o is the pre-exponential factor in moles $\text{m}^{-2} \text{s}^{-1}$; E_a is the activation energy in kcal mole^{-1} ; X_m is the fraction of oxygen in a given mineral phase; c_m and f_m are empirical constants used to estimate the equilibrium temperature-dependent fractionation factor for the m^{th} oxygen-bearing mineral phase using the following relationship: $10^3 \ln(\alpha_m) = \frac{10^3 c_m}{(T+273.15)^3} + \frac{10^6 d_m}{(T+273.15)^2} + \frac{10^9 e_m}{(T+273.15)} + f_m$. The bulk equilibrium fractionation factor for a given lithologic unit (α_{rk}) in our model

is given by $\alpha_{rk} = \sum_{m=1}^M f_m \alpha_m$ where f_m is the fraction of the m^{th} oxygen-bearing mineral phase that occurs within a given lithologic unit. *Zhang *et al.* (1994); †Zheng (1999); ‡Sheppard & Gilg (1996).

Table 4 Initial percentage of oxygen-bearing minerals in each stratigraphic layer.

Unit Numbers	Unit name	Qtz	Dol	Cal	Kaol	Bar	Anor
10	Fault zone	75	5	—	10	10	—
9	Quaternary basin fill	36	5	50	—	—	9
8	Volcanoclastics (Tuffs, alluvium)	36	5	50	—	—	9
7	Middle Miocene volcanics	70	—	—	20	—	10
6	High-permeability karst unit	—	10	80	10	—	—
5	Low-permeability carbonates	—	10	80	10	—	—
4	Low-permeability proterozoic siliciclastics	75	5	—	19	1	—
3	High-Permeability proterozoic siliciclastics	75	5	—	19	1	—
2	Low-permeability proterozoic siliciclastics	75	5	—	19	1	—
1	Proterozoic metamorphic rocks	80	—	—	5	—	15

Qtz, Quartz; Dol, Dolomite; Cal, Calcite; Kaol, Kaolinite; Ba, Barite; Anor, Anorthite.

condition was imposed ($dT/dz = 0$). This boundary condition implies that vertical flow rates are high enough that heat is not lost by conduction at the water table. This boundary condition was used by Appold *et al.* (2007) to emulate spring discharge along Reguio-Carneos and Coast faults in the Santa Barbara Basin. A basal heat flux was also imposed at the base of the solution domains (80 mW m^{-2}), based on heat flux estimates from the Northern Nevada Rift (Blackwell 1983). We fixed the $\delta^{18}\text{O}$ composition of meteoric recharge at -15‰ at the water table. A no-flux boundary condition was imposed ($dR_f/dz = 0$) at the Malpais fault zone for these two tracers. No-flux boundary conditions were imposed along the sides and base of the solution domain for isotope transport.

Thermal conductivity, solute diffusivity, longitudinal and transverse dispersivities were fixed (Table 5) for all lithological units. We assumed a conductive geothermal

gradient as an initial condition (about 40°C km^{-1}). Initial fluid isotope composition (R_f) values were assigned using these initial conductive temperatures. Each stratigraphic unit was assigned an initial rock isotope composition depending on its mineral assemblages (Table 4).

Hydrostratigraphic framework model

The permeabilities of the hydrostratigraphic units shown in Fig. 2B are listed in Table 6. The permeability values used in our model are consistent with values reported in the literature for Basin and Range sedimentary rocks (Blankenship & Weir 1973; Winograd & Thordarson 1975; Plume & Carlton 1988; Maurer *et al.* 1996; Bredehoeft 1997; Belcher 2004; Welch *et al.* 2007). We used published permeability data sets for crustal rocks as a guide in selecting these values (Brace 1980, 1984; Clauser 1992; Manning & Ingebritsen 1999). Because these data sets present a range of permeability conditions for a given lithologic unit, we relied on model calibration to match Beowawe heat-flow and temperature profiles (Person *et al.* 2008). The hydrogeologic section includes the following hydrogeologic units: a deep, low-permeability unit that includes Proterozoic crystalline basement rocks (Unit 1; dark blue strata in Fig. 2B); two low-permeability intervals of Upper Proterozoic to Early Cambrian siliciclastic rocks (Units 2, 4; green strata in Fig. 2B) that bracket a middle 1.5-km-thick interval of higher permeability, highly fractured quartz sandstone (Unit 3; white unit in Fig. 2B); Cambrian–Devonian dominantly carbonate rocks (Unit 5, purple strata in Fig. 2B); low-permeability strata of the Roberts Mountain allochthon (Unit 7, orange strata in Fig. 2B); Miocene volcanic rocks, including lava flows and ash-flow tuff (Unit 8, brown strata in Fig. 2B); alluvial basin fill (Unit 9, yellow strata in Fig. 2B), and fault zones (Unit 10, red lines in Fig. 2B). A one-hundred-meter-thick interval of potentially enhanced horizontal permeability was added at the top of the Paleozoic carbonate unit (Unit 6, blue interval in Fig. 2B). This interval represents a sequence boundary that

Table 5 Rock thermal and transport properties.

Variable	Symbol	Value/Units
Thermal conductivity of fluid	λ_s	0.58 W-m/ $^{\circ}$ C
Thermal conductivity of solids	λ_s	2.5 W-m/ $^{\circ}$ C
Heat capacity of the fluid phase	c_f	4180 J kg $^{-1}$
Heat capacity of the solid phases	c_s	800 J kg $^{-1}$
Longitudinal dispersivity	α_L	1.0 m
Transverse dispersivity	α_T	0.1 m
Solute diffusivity	D_d	10 $^{-10}$ m 2 s $^{-1}$
Reactive surface areas	\bar{A}	10 $^{-4}$ m 2 mole $^{-1}$

Table 6 Hydrologic rock properties.

Unit	log $_{10}$ (k)	Description
10	–11 to –13	Faults (Black lies)
9	–16	Basin fill (Yellow)
8	–17	Tuffs (Brown)
7	–17	Volcanics (Orange)
6	–10	Karst zone (Blue)
5	–17	Carbonates (Purple)
4	–17	Proterozoic siliciclastics (Green)
3	–14	Proterozoic shales (White)
2	–17	Proterozoic sandstones (Green)
1	–17	Proterozoic bed rocks (Dark Blue)

k_x (horizontal permeability, m 2), Unit numbers are listed in Fig. 2B.

commonly contains karst features and is highly permeable. Such sequence boundaries are present at various stratigraphic levels within the Paleozoic section (Cook & Corboy 2004). The inferred subsurface structural geometry portrayed on section a-a' is generalized from published sections presented in John & Wrucke (2003) and in Watt *et al.* (2007). Major structural elements include west-dipping range-bounding faults on the west side of the Shoshone Range, and steep faults in the vicinity of the Mule Canyon deposit that proxy for the east-dipping Muleshoe fault (John *et al.* 2003) and for highly anisotropic permeability within dike swarms of the northern Nevada rift (John & Wrucke 2003). A single steep west-dipping fault is portrayed in the vicinity of Beowawe and generalizes the Malpais fault and other ENE-trending and NNW-trending faults that localize geothermal fluids (Zoback 1979; Struhsacker 1980). All of these faults are portrayed as cutting both low-permeability strata of the Roberts Mountain allochthon and underlying Cambrian–Devonian dominantly carbonate rocks. Gentle dips result in the most permeable part of the Paleozoic carbonate-rock section, only attaining maximum depths of about 6 km below land surface.

The subvertical faults are relatively thin (approximately 40 m) and are assigned isotropic fault properties. Subvertical faults are connected hydrologically to a thin aquifer unit at the top of the Paleozoic carbonates and, potentially, by a deep, thick, more porous aquifer in the middle of the siliciclastic sequence (10 $^{-13}$ m 2). Practical

considerations regarding simulation time restricted our ability to represent the fault zones using grid refinement on the submeter scale, which would have been desirable.

Sensitivity study

We conducted a sensitivity study to assess what values of fault permeability could explain the modern temperature overturns as well as the isotopic evolution of geothermal discharge. We ran the simulations using fault permeabilities ranging from 10 $^{-14}$ to 10 $^{-11}$ m 2 . Computed temperatures simulated using fault permeability <10 $^{-13}$ m 2 were clearly too low and are not presented. Computational limitations prevented us from running simulations with fault permeabilities <10 $^{-11}$ m 2 . After 5000 years of hydrothermal fluid flow, we lowered the subvertical fault and karst reservoir permeability to 10 $^{-19}$ m 2 to allow the system to return to conductive equilibrium. This was done to represent the effects of fault clogging by silica mineralization. We then monitored the thermal and isotopic recovery for an additional 5000 years. The rationale for including a thermal-recovery phase was to see whether the fluids could return to isotopic equilibrium after 5000 years. We monitored simulated temperatures at the base of the Muleshoe fault in the recharge area and at the water table along the Malpais fault within the discharge area.

RESULTS

Isotopic composition and age of the sinter deposits

Calculated $\delta^{18}O_{H_2O}$ values and ^{14}C dates on pollen recovered from sinter samples provide evidence for two periods of geothermal fluid discharge that each exhibit a progressive decrease in $\delta^{18}O_{H_2O}$ through time (Fig. 3). Some of our data are from a single flow-stone layer extending downslope from a vent lacks the progressive changes that might be expected if Rayleigh fractionation during progressive precipitation of silica was important. The highest $\delta^{18}O_{H_2O}$ values reflect isotopic exchange between fluid and sedimentary rocks in a geothermal reservoir at low water/rock ratios (e.g., 0.1) and temperatures in excess of 200 $^{\circ}$ C (Sheppard 1986). The trends of decreasing $\delta^{18}O_{H_2O}$ through time suggest increasing contributions of unexchanged meteoric water. Modern geothermal fluids at Beowawe have an isotopic composition ($\delta^{18}O_{H_2O} = -16.5\text{‰}$, $\delta D = -120\text{‰}$) (John *et al.* 2003) that is representative of unexchanged meteoric water and that plots near (within 4 $‰$ $\delta^{18}O$) the meteoric water line.

Model results

For a fault permeability of 10 $^{-12}$ m 2 , computed temperatures after 200 years (Fig. 7A) show strong convective

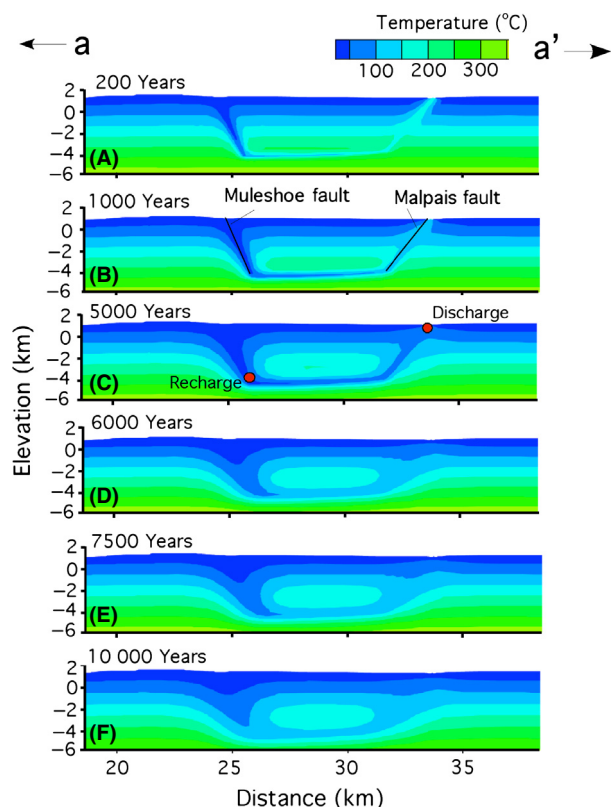


Fig. 7. Computed temperature contour maps illustrating thermal evolution along the Malpais fault, Muleshoe fault, and karst aquifer. Fault zones were assigned a uniform permeability of 10^{-12} m^2 . Fluid flow is active for 5000 years (A–C) followed by 5000 years (6000–10 000 years; D–F) of conductive cooling. Shallow meteoric fluid infiltration occurs down the Muleshoe fault zone and then along a thin, permeable karst zone. Upflow occurs along the Malpais fault zone. Points labeled 'recharge' and 'discharge' are the locations within the Beowawe geothermal system where temperature and $\delta^{18}\text{O}_{\text{fluid}}$ were plotted through time in Fig. 8A–D.

cooling within the recharge area along the Muleshoe fault. By 1000 years, temperature declines extend into the karst aquifer and pronounced thermal overturns developed (Fig. 7B). The rate of cooling within the Muleshoe fault is strongly controlled by fault permeability (Fig. 8A). Within the discharge area along the Malpais fault, temperatures increased to a peak value about 180°C before declining (Fig. 8C). The timing of peak discharge temperature along the Malpais fault zone is quite sensitive to fault permeability (Fig. 8C). For a fault permeability of 10^{-13} m^2 , the temperatures peaked after about 5000 years whereas for a fault permeability of 10^{-11} m^2 , they peaked in <100 years. A fault permeability of $10^{-12.3} \text{ m}^2$ ($5.0 \times 10^{-13} \text{ m}^2$) produced peak temperatures of about 180°C after 1000 years. The highest permeability fault zone did not correspond to the highest discharge temperature because of the cooling effect of low-temperature meteoric water (Forster & Smith 1989). Vertical flow rates along the Malpais fault varied between about 60 and 3 m year^{-1} for the range of

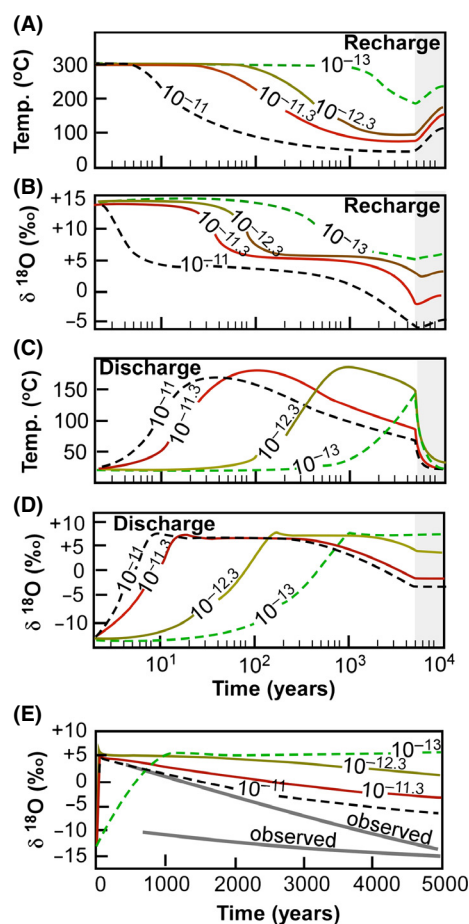


Fig. 8. Effect of fault-permeability variations on simulated temporal temperature changes (A) and (B) oxygen isotopic composition along the Muleshoe fault zone at a depth of about 5 km. The numbers on the lines denote the permeability assigned to the Muleshoe and Malpais faults, in m^2 . Effect of fault-permeability variations on simulated temporal changes in temperature (C) and (D) oxygen isotopic composition along the Malpais fault zone at the water table. The shaded area of the graphs represents conductive recovery following 5000 years of convection and cooling of fluids moving through the system. Locations within the recharge and discharge area are shown in Fig. 8C (red circles). (E) Comparison of observed trends (gray lines) and computed changes in $\delta^{18}\text{O}_{\text{H}_2\text{O}}$ versus time for the Beowawe sinter terrace.

permeabilities considered (10^{-11} to 10^{-13} m^2). We estimate that for this range of fault permeabilities, the time required for ground water to pass through the single-pass system by pure advection is between 300 and 4500 years.

When the flow system is shut off at 5000 years, a relatively cool region with a vertical width of 1000 m is present above and below the karst zone (Fig. 7C). Conductive thermal recovery is much slower rate than the advective cooling (Fig. 7D–F, 8A). This prevented the recovery back to initial thermal conditions over a 5000-year period and slows temperature-dependent isotopic exchange rates (Fig. 8B, 8D). Based on the vertical thickness of the thermally disturbed region above and below

the karst zone (1000 m), we estimate that it would require at least 10^4 additional years to approach initial conductive conditions, assuming a thermal diffusivity of $1.25 \times 10^{-6} \text{ m}^2 \text{ s}^{-1}$. If the flow system was reinitiated following the 5000-year period of conductive recovery, the discharging fluid along the Malpais fault zone would be only moderately enriched.

Fig. 4E–G presents computed, time-dependent evolution of temperature profiles extracted from our cross-sectional model at different distances from the Malpais fault. Early-time (200–1000 years since the onset of flow) temperature profiles within the hanging wall close to the Malpais fault resulted in temperature overturns that are similar in form to observed conditions within the Batz-1 and 85-15 wells (Fig. 4E–G). The timescale is much shorter than the geochemical transients inferred from the sinter deposits (Fig. 3).

By 5000 years, fluid temperatures were below 100°C at a depth of 5 km for the most permeable fault scenarios (Fig. 8A). These lower temperatures restrict isotopic fluid–rock interactions. Once the flow system ceased at 5000 years, computed temperatures within the recharge area along the Muleshoe fault rebounded toward their initial conditions (Fig. 7D–F; Fig. 8). Computed $\delta^{18}\text{O}_{\text{H}_2\text{O}}$ composition within the recharge area along the Muleshoe fault underwent rapid initial depletion as meteoric water began to descend (Fig. 8B). As progressively lighter fluids invaded the fault zone, reaction rates increased under isothermal conditions, causing stabilization in $\delta^{18}\text{O}_{\text{H}_2\text{O}}$ levels. The amount of isotopic depletion depends strongly on permeability. The isotopic composition of fluids entering the karst aquifer was lightest for the most permeable conditions. Isotopic enrichment between the bottom of the Muleshoe fault zone and the discharge area at the top of the Malpais fault was only slight (approximately 2 ‰ Fig. 8D). Enrichment in the isotopic composition in the discharge area (Fig. 8D) along the Malpais fault peaked earlier than computed temperatures (Fig. 8C). Computed $\delta^{18}\text{O}_{\text{H}_2\text{O}}$ composition dropped from about +6 to –3 ‰ but never reached the meteoric water end member (–15 ‰ $\delta^{18}\text{O}$). The slight bump in the initial peak of $\delta^{18}\text{O}_{\text{H}_2\text{O}}$ is due to a downward tilt in the karst reservoirs to the west; the initial isotopic composition along the west edge of the karst zone was slightly enriched relative to the east side.

The time required for the simulated $\delta^{18}\text{O}_{\text{H}_2\text{O}}$ composition within the Malpais fault zone to peak (+7 ‰) ranged between 10 and 1000 years after the onset of flow, for the permeability conditions considered (Fig. 8D). These values are more depleted than the initial equilibrium conditions with the karst reservoir at 5 km depth (+13 ‰), likely because of mixing of relatively unexchanged meteoric water and carbonate reservoir fluids along the flow path. Simulated oxygen-isotope composition of the discharging fluids decreased from about +7 to –3 ‰ for fault permeabilities

between 10^{-12} and 10^{-11} m^2 (Fig. 8D). This is about 50% of the decline observed (Fig. 3, Fig. 8E). Once flow terminated, recovery of computed temperatures (Fig. 8A) and $\delta^{18}\text{O}_{\text{H}_2\text{O}}$ began (Fig. 8B). However, the fluid isotopic composition did not return to equilibrium levels over the simulated time frame due to the slow rates of thermal recovery.

DISCUSSION AND CONCLUSIONS

Our cross-sectional, single-pass model is clearly too idealized to account for all features of the observed thermal and isotopic data. To match the observed thermal overturns in temperature profiles near the Malpais fault (Fig. 4B–C), the model requires that hydrothermal fluid flow persists for only 1000 years or less. This is much briefer than the duration of declining isotopic composition within the sinter deposits we sampled (5000–7000 years). How can these two observations be reconciled? We propose that the Malpais fault zone is composed of several pathways to the surface, each pathway having different fault zone apertures. As the most permeable conduit is sealed off by mineralization, alternative conduits are accessed along the Malpais fault. This is somewhat analogous to channel avulsion in braided river systems. Published timescale estimates for fault clogging by Lowell *et al.* (1993) support this conceptual model. These authors developed simple analytical models for fault sealing by silica precipitation using a wide range of fault permeabilities (10^{-10} to 10^{-16} m^2) and geothermal reservoir temperatures (50°C and 300°C). For these two temperatures, the time required for fault sealing ranged from <1 year (300°C) to over 300 years (50°C) for a fault permeability of 10^{-12} m^2 . The notion of changes in the locus of hot spring discharge is supported, in part, by the observation that peak shallow heat flow today is to the south of the Beowawe sinter deposits, which was clearly the locus of discharge in the past (Fig. 2A). This conceptual model of fault clogging and rerouting of flow through fault zones is not a new idea. Saffer (2015) present thermal/geochemical data from the Barbados and Nankai accretionary prism to argue that relatively high rates of fluid fluxes through permeable fault systems could only be active for between 0.2 and 10% of the time due to clogging by fluid–rock geochemical reactions (Saffer 2015, Fig. 4C).

Another complexity that is not accounted for in our single-pass model is the observed abrupt shift from nearly meteoric fluid composition (–15‰ $\delta^{18}\text{O}$) at about 7.5 ka to isotopically enriched discharge at 4.5 ka. We speculate that different reservoirs may be tapped during different seismic events. Alternatively, the conflict between modeled and measured values might be resolved if the discharging geothermal fluids are actually part of a two-component

mixture of a deeper, slowly circulating, hot fluid with enriched $\delta^{18}\text{O}$ and a shallow-circulating, warm fluid meteoric fluid with lighter $\delta^{18}\text{O}$. The fault rupture might preferentially alter the permeability of the deeper part of the fault, and thus, increase the amount of deeper fluid in discharging water. After fault slip, the deeper portion of the fault might 'heal up' and gradually decrease the deeper fluid contribution to very low levels, while the shallow fluid contribution might remain more constant. Thus, the deeper fluid temperature and $\delta^{18}\text{O}$ oscillate only moderately with time (and could perhaps fully recover between earthquakes).

Our interpretation of the thermal and isotopic evolution of the Beowawe geothermal system must be tempered by parameter uncertainty. There is a significant uncertainty in the reactive surface area and kinetic coefficients used in our fluid–rock isotope-exchange models. Surface area for fluid–rock isotope-exchange models can be computed using mineral grain size (Brantley & Mellott 2000) or fracture spacing (Rimstidt & Barnes 1980). Surface areas based on mineral grains can be as high as $1 \text{ m}^2 \text{ mole}^{-1}$. The value we used ($10^{-4} \text{ m}^2 \text{ mole}^{-1}$) was based on fracture spacing and would be representative of a fracture spacing of about 70 cm (assuming the rock is comprised entirely of feldspar). Our model of fault permeability was static. Other studies (Roberts *et al.* 1996; Garven *et al.* 2001; Appold *et al.* 2007) have allowed fault permeability to decay through time due to changes in fault stress, mineralization, and fluid pressure decline.

For a fault permeability of 10^{-12} m^2 , our model results indicate that discharge peaked at temperatures of 180°C along the Malpais fault about 30 years after the onset of convection. Then, discharge temperatures began to cool. The most isotopically enriched discharge fluids break through in about 10 years. The finding of transient heat pulses at hot springs is not new. Numerous researchers have observed similar phenomena in their models of fault-controlled hydrothermal systems (e.g., Forster & Smith 1989; Lopez & Smith 1995). This is due to the high rate of enthalpy extraction allowed by the high fault permeability and consequent high flow rates. It is worth noting that the magnitude of the temperature change presented in this study is far larger than observed in studies of modern earthquake-influenced hot springs (e.g., Mogi *et al.* 1989; Rowland *et al.* (2008)). This may be due to the extraordinary high extensional deformation rates along the Basin and Range faults (Kennedy & van Soest 2007).

Our oxygen-isotope analysis of ^{14}C -dated sinter deposits (Fig. 3) shows that large (up to 20‰) time-dependent decreases in the isotopic composition of the geothermal fluids occurred along the Malpais fault zone over geologic timescales. We interpret this decline as the result of progressive influx of meteoric fluids into a single-pass, liquid-dominated, geothermal system. Other potential

mechanisms that could account for isotopic changes (e.g., boiling, climate-driven changes in precipitation composition and isotopic composition during the late Pleistocene, or Rayleigh distillation of the geothermal fluids during sinter deposit formation) cannot account for such a large shift in $\delta^{18}\text{O}$. The single-pass hydrothermal/isotope transport model of the Beowawe geothermal system seems to be the most plausible mechanism for the observed data, although it is clearly too idealized. If our conceptual model of the Beowawe geothermal system is correct, our analysis provides insights into how transient permeability changes occur along fault zones over geological timescales. Estimated rates of silica clogging of faults (as fast as 10 years; Lowell *et al.* 1993) are much shorter than those indicated by the sinter-deposit isotope data.

Groundwater flow must be three-dimensional in nature. Person *et al.* (2012) showed how hydrothermal flow frequently focuses at relatively high-permeability intersections of fault zones, as observed across the Basin and Range by Coolbaugh *et al.* (2005). Further, Garg *et al.* (2007) found that only narrow regions of the Malpais fault zone were permeable. Nevertheless, any three-dimensional model must still incorporate downward fluid movement on the Muleshoe or some other fault system, lateral flow through a reservoir, and upward flow along the Malpais fault.

Other studies have described transient hydrothermal systems within the Basin and Range. McKenna *et al.* (2005) concluded that the high temperatures (280°C at 3.8 km depth) along the base of the Stillwater fault within the Dixie Valley geothermal system must be due to hydrothermal flow transients on the order of 30 000–50 000 years. These authors also speculated that the time-dependent fault permeability was related to seismicity. Temperature profiles from wells at Dixie Valley, however, show little evidence of thermal overturns.

Low-magnitude earthquakes result in slip increments of millimeters to centimeters along faults. Hill (1977) and Sibson (1996) proposed that low-magnitude (<4M) earthquake swarms can induce significant amounts of fluid movement capable of generating economic gold deposits along fracture networks. Varying the permeability of the fault zones in our model provided some insight into the magnitude of permeability change following each seismic event. While none of the models produced the full 20‰ range observed in Fig. 3, the fault permeability had to have been on the order of 10^{-11} m^2 or greater. The highest permeability scenario ($5 \times 10^{-11} \text{ m}^2$) produced about a 10‰ decrease in $\delta^{18}\text{O}_{\text{H}_2\text{O}}$ over a few thousand years while a permeability of 10^{-13} m^2 produced almost no decrease (Fig. 8D). Numerical considerations prevented us from assigning higher fault permeability to the Muleshoe and Malpais faults. It is possible that representing isotope transport through distinct fractures, or greater mesh refine-

ment, would have improved the model fit to observed data. Extrapolating the trends in the rate of decline in computed $\delta^{18}O_{H_2O}$ in Fig. 8E, we suspect that a fault permeability of 10^{-9} m^2 would likely produce a close match with observed data. Prior to the onset of hydrothermal circulation, the permeability of the Malpais and/or Muleshoe fault must have been at or below 10^{-14} m^2 , producing low-temperature discharge that could not have carried much dissolved silica to form sinter deposits. Fault conductance controls the magnitude of convective heat flow, so our reported fault permeabilities are to some degree non-unique. A wider fault zone would require a lower fault permeability to produce the same convective thermal anomaly.

Isotope data collected as part of this study suggest that Holocene geothermal systems in the Basin and Range Province are episodic in nature on timescales of about 5000–7000 years. Zoback (1979) estimated that about 210 000 years were required to account for all of the silica ($1.28 \times 10^{11} \text{ kg}$) along the Beowawe geyser field terrace. She assumed continuous flow at modern Beowawe geyser field discharge rates (61 l s^{-1}) and modern silica concentrations. In our model, each hydrothermal flow event discharged about $9.1 \times 10^9 \text{ kg}$ of silica (Person *et al.* 2008). Assuming a fault zone width of 40 m, a length of 2 km, and that 10% of the dissolved silica is available for sinter formation, over 100 episodic flow events would be required to form the $1.28 \times 10^{11} \text{ kg}$ Beowawe geyser field sinter terrace.

ACKNOWLEDGEMENTS

We thank Andy Manning of the USGS and two anonymous reviewers for their constructive criticism of an earlier draft of this manuscript. This work was supported by a NSF grant to Mark Person and Albert Hofstra (NSF-EAR 0809644). We also acknowledge support under a National Science Foundation (EPSCoR) under Grant No. IIA-1301346 to Mark Person and Laura Crossey.

REFERENCES

- Appold MS, Garven G, Boles JR, Eichhubl P (2007) Numerical modeling of the origin of calcite mineralization in the Refugio-Carneros fault, Santa Barbara Basin, California. *Geofluids*, **7**, 79–95.
- Asmerom Y, Polyak V, Burns S (2010) Variable winter moisture in the southwestern United States linked to rapid glacial climate shifts. *Nature Geoscience*, **3**, 114–117.
- Baertschi P, Silverman SR (1951) The determination of relative abundances of the oxygen isotopes in silicate rocks. *Geochemica et Cosmochimica Acta*, **1**, 317–328.
- Batzle M, Wang Z (1992) Seismic properties of pore fluids. *Geophysics*, **57**, 1396–1408.
- Belcher WR (2004) Death Valley regional ground-water flow system, Nevada and California—Hydrogeologic framework and transient ground-water flow model. US Geological Survey Scientific Investigation Series Report, 1171, 408.
- Blackwell DD (1983) Heat flow in the northern Basin and Range province. In *The Role of Heat in the Development of Energy and Mineral Resources in the Northern Basin and Range Province*. Geothermal Resources Council Special Report, **13**, 81–93.
- Blankennagel RK, Weir JE Jr (1973) Geohydrology of the eastern part of Pahute Mesa, Nevada Test Site, Nye County, Nevada. US Geological Survey Professional Paper 712–B, 35.
- Boles JR, Grivetti M (2000) Calcite cementation along the Refugio/Carneros fault, coastal California: a link between deformation, fluid movement and fluid-rock interaction at a basin margin. *Journal of Geochemical Exploration*, **69–70**, 313–316.
- Boles JR, Eichhubl P, Garven G, Chen J (2004) Evolution of a hydrocarbon migration pathway along basin-bounding faults: evidence from fault cement. *American Association of Petroleum Geologists Bulletin*, **88**, 947–970.
- Borthwick J, Harmon RS (1982) A note regarding ClF3 as an alternative to Br F5 for oxygen isotope analysis. *Geochemica et Cosmochimica Acta*, **46**, 1665–1668.
- Bowman JR, Willett SD, Cook SJ (1994) Oxygen isotopic transport and exchange during fluid flow: one-dimensional models and applications. *American Journal of Science*, **294**, 1–55.
- Brace WF (1980) Permeability of crystalline and argillaceous rocks. *International Journal of Rock Mechanics and Mining Science*, **17**, 241–245.
- Brace WF (1984) Permeability of crystalline rocks: new in situ measurements. *Journal of Geophysical Research*, **89**, 4327–4330.
- Brantley S, Mellott N (2000) Surface area and porosity of primary silicate minerals. *American Mineralogist*, **85**, 1767–1783.
- Bredehoeft JD (1997) Fault permeability near Yucca Mountain. *Water Resources Research*, **33**, 2459–2463.
- Broadsky EE, Roeloffs E, Woodcock D, Gall I, Manga M (2003) A mechanism for sustained groundwater pressure changes induced by distant earthquakes. *Journal of Geophysical Research*, **108**, 1–10.
- Chia Y, Wang YS, Chiu JJ, Liu WW (2001) Changes of groundwater level due to the 1999 chi-chi earthquake in the Choshui river alluvial fan in Taiwan. *Bulletin of the Seismological Society of America*, **91**, 1062–1068.
- Clauser C (1992) Permeability of crystalline rocks. *EOS, Transactions of the American Geophysical Union*, **73**, 233–240.
- Cook HE, Corboy J (2004) Great Basin Paleozoic carbonate platform; facies, facies transitions, depositional models, platform architecture, sequence stratigraphy, and predictive mineral hosts models. US Geological Survey Open-File Report, 2004–1078, 135.
- Coolbaugh MF, Arehart GB, Faulds JE, Garside LJ (2005) Geothermal systems in the Great Basin, western United States: modern analogues to the roles of magmatism, structure, and regional tectonics in the formation of gold deposits. In: *Geological Society of Nevada Symposium 2005: Window to the World* (eds Rhoden HN, Steininger RC, Vikre PG), pp. 1063–1082. Nevada Geological Society, Reno, NV.
- Curewitz D, Karson J (1994) Structural settings of hydrothermal outflow: fracture permeability maintained by fault propagation and interaction. *Journal of Volcanology and Geothermal Research*, **79**, 149–168.
- Day GA (1987) Source of recharge to the Beowawe geothermal system, Nevada. University of Nevada Reno Thesis, p. 82.
- Dziak RP, Chadwick WW, Christopher GG, Embley RW (2003) Hydrothermal temperature changes at the southern Juan de Fuca Ridge associated with MW 6.2 Blanco Transform earthquake. *Geology*, **31**, 119–122.

- Elkhoury JE, Brodsky EE, Agnew DC (2006) Seismic waves increase permeability. *Nature*, **441**, 1135–1138.
- Faulder DD, Johnson SD, Benoit WR (1997) Flow and permeability structure of the Beowawe, Nevada hydrothermal system, in *Proceedings, Twenty-Second Workshop on Geothermal Research and Engineering*: Stanford, California. Stanford University Report, SGP-TR-155, 63–73.
- Fogg G, Senger RL (1985) Automatic generation of flow nets with conventional ground-water modeling algorithms. *Groundwater*, **23**, 336–344.
- Forster C, Smith L (1989) The influence of groundwater flow on thermal regimes in mountainous terrain: a model study. *Journal of Geophysical Research*, **94**, 9439–9451.
- Friedrich AM, Lee J, Wernicke BP, Sieh K (2004) Geologic context of geodetic data across a Basin and Range normal fault, Crescent Valley, Nevada. *Tectonics*, **23**, 1–24.
- Garg SK, Pricheet JW, Wannamaker PE, Combs J (2007) Characterization of geothermal reservoirs with electrical surveys: beowawe geothermal field. *Geothermics*, **36**, 487–517.
- Garven G, Bull SW, Large RR (2001) Hydrothermal fluid flow models of stratiform ore genesis in the McArthur Basin, Northern Territory, Australia. *Geofluids*, **1**, 289–311.
- Harris C (1989) Oxygen-isotope zonation of agates from Karoo volcanics of the Skeleton Coast, Namibia. *American Mineralogist*, **74**, 476–481.
- Heimgartner M, Louie JN, Scott JB, Thelen W, Lopez CT, Coolbaugh M (2006) The crustal thickness of the great basin: using seismic refraction to assess regional geothermal potential. *Geothermal Resources Council Transactions*, **30**, 83–86.
- Herdianita NR, Rodgers KA, Browne PRL (2000) Routine instrumental procedures to characterise the mineralogy of modern and ancient silica sinters. *Geothermics*, **29**, 65–81.
- Hill DP (1977) A model for earthquake swarms. *Journal of Geophysical Research*, **82**, 1347–1352.
- Hofstra AH, Cline JS (2000) Characteristics and models for Carlin-type gold deposits. *Reviews in Economic Geology*, **13**, 163–220.
- Hurwitz S, Lowenstern JB, Heasler H (2007) Spatial and temporal geochemical trends in the hydrothermal system of Yellowstone National Park: inferences from river solute fluxes. *Journal of Volcanology and Geothermal Research*, **162**, 149–171.
- Husen S, Taylor R, Smith RB, Heasler H (2004) Changes in geyser eruption behavior and remotely triggered seismicity in Yellowstone National Park produced by the 2002 M 7.9 Denali fault earthquake, Alaska. *Geology*, **32**, 537–540.
- John DA, Wrucke CT (2003) Geologic map of the mule canyon quadrangle, Lander County, Nevada. *Nevada Bureau of Mines and Geology Map*, **144**, 18.
- John DA, Hofstra AH, Fleckv RJ, Brummer JE, Saderholm EC (2003) Geologic setting and genesis of the mule canyon low-sulfidation epithermal gold-silver deposit, North-Central Nevada. *Economic Geology*, **98**, 425–463.
- Kennedy BM, van Soest MC (2007) Flow of mantle fluids through the ductile lower crust: helium isotope trends. *Science*, **318**, 1433–1436.
- Kim ST, O'Neil JR (1997) Equilibrium and nonequilibrium oxygen isotope effects in synthetic carbonates. *Geochimica et Cosmochimica Acta*, **61**, 3461–3475.
- King C-Y, Basler D, Presser TS, Evans CW, White LD, Minissale AD (1994) In search of earthquake-related hydrologic and chemical changes along the Hayward fault. *Applied Geochemistry*, **9**, 83–91.
- King CY, Azuma S, Igarashi G, Ohno M, Saito H, Wakita H (1999) Earthquake-related water level changes at 16 closely clustered wells in Tono, central Japan. *Journal of Geophysical Research*, **104**, 13073–13082.
- Kita I, Taguchi S, Matsubaya O (1985) Oxygen isotope fractionation between amorphous silica and water at 34–93 C. *Nature (London)*, **314**, 83–84.
- Lopez DL, Smith L (1995) Fluid flow in fault zones: analysis of the interplay of convective circulation and topographically driven groundwater flow. *Water Resources Research*, **31**, 1489–1503.
- Lowell RP (1991) Modeling continental and submarine hydrothermal systems. *Reviews of Geophysics*, **29**, 457–476.
- Lowell R, Van Cappellen P, Germanovich LN (1993) Silica precipitation in fractures and the evolution of permeability in hydrothermal upflow zones. *Science*, **260**, 192–194.
- Lynn BA, Campbell KA, Moore J, Brown PRL (2008) Origin and evolution of the Steamboat Springs siliceous Sinter deposit, Nevada, U.S.A. *Sedimentary Geology*, **210**, 111–131.
- Manga M, Rowland JC (2009) Response of Alum Rock springs to the October 30, 2007 earthquake and implications for the origin of increased discharge after earthquakes. *Geofluids*, **9**, 237–250.
- Manga M, Beresnev I, Brodsky EE, Elkhoury JE, Elsworth D, Ingebritsen SE, Mays DC, Wang CY (2012) Changes in permeability caused by transient stresses: field observations, experiments, and mechanisms. *Reviews of Geophysics*, **50**, 1–24.
- Manning C, Ingebritsen SE (1999) Permeability of the continental crust. The implications of geothermal and metamorphic systems. *Reviews of Geophysics*, **37**, 127–150.
- Mariner RH, Presser TS, Evans WC (1983) Geochemistry of active geothermal systems in the Northern Basin and Range Province. Special Report, Geothermal Resources Council Special Report, 13, 95–119.
- Maurer DK, Plume RW, Thomas JM, Johnson AK (1996) Water resources and effects of changes in ground-water use along the Carlin Trend, north-central Nevada. United States Geological Survey Water Resources Investigations Report, 96-4134, 146.
- McKenna JR, Blackwell DD, Richards MC (2005) Natural state modeling, structure, preliminary temperature and chemical synthesis of the Dixie Valley, Nevada Geothermal System, Proceedings. Thirtieth Workshop on Geothermal Reservoir Engineering, Stanford University, Stanford, California, January 31–February 2, 2005, Stanford University Report, SGP-TR-176.
- Mogi K, Mochizuki H, Kurokawa Y (1989) Temperature changes in an artesian spring at Usami in the Izu Peninsula (Japan) and their relation to earthquakes. *Tectonophysics*, **159**, 95–108. doi:10.1016/0040-1951(89)90172-8.
- Muir-Wood R, King G (1993) Hydrological signatures of earthquake strain. *Journal of Geophysical Research*, **98**, 22035–22068.
- Nolan TB, Anderson GH (1934) The geyser area near Beowawe, Eureka County, Nevada. *American Journal of Science*, **27**, 215–229.
- Olmsted FH, Rush FE (1987) Hydrogeologic reconnaissance of the Beowawe geysers geothermal area, Nevada. *Geothermics*, **16**, 27–46.
- Person MA, Banerjee A, Hofstra AH, Sweetkind DS, Gao Y (2008) Hydrologic models of modern and fossil geothermal systems in the Great Basin: genetic implications for epithermal Au-Ag and Carlin-type gold deposits. *Geosphere*, **4**, 888–917.
- Person M, Hofstra A, Sweetkind D, Stone W, Cohen D, Gable C, Banerjee A (2012) Analytical and numerical models of hydrothermal fluid flow at fault intersections. *Geofluids*, **12**, 312–326.
- Plume RW, Carlton SM (1988) Hydrogeology of the Great Basin region of Nevada, Utah, and adjacent states. *United States*

- Geological Survey Hydrologic Investigations Atlas*, HA-694-A, scale 1:100 000.
- Raffensperger JP, Garven G (1995) The formation of unconformity-Type uranium ore deposits, 1: coupled groundwater flow and heat transport modeling. *American Journal of Science*, **95**, 581–636.
- Renner JL, White DE, Williams DL (1975) Hydrothermal convection systems in assessment of geothermal resources of the United States 1975. *United States Geological Survey Circular*, **726**, 5–57.
- Rimstidt JD, Barnes HL (1980) The kinetics of silica-water reactions. *Geochimica et Cosmochimica Acta*, **44**, 1683–1699.
- Rimstidt JD, Cole DR (1983) Geothermal mineralization I: the mechanism of formation of the Beowawe, Nevada, siliceous sinter deposit. *American Journal of Science*, **283**, 861–875.
- Roberts SJ, Nunn JA, Cathles LM, Cipriani F-D (1996) Expulsion of abnormally pressured fluids along faults. *Journal of Geophysical Research*, **101**, 231–252.
- Rojstaczer S, Wolf W (1992) Permeability changes associated with large earthquakes: an example from Loma Prieta, California. *Geology*, **20**, 211–214.
- Rowland JC, Manga M, Rose TP (2008) The influence of poorly interconnected fault zone flow paths on spring geochemistry. *Geofluids*, **8**, 93–101.
- Saffer D (2015) The permeability of active subduction plate boundary faults. *Geofluids*, **15**, 193–215.
- Sheppard SMF (1986) Characterization and isotopic variations in natural waters, Chapter 6. In: *Stable Isotopes in High Temperature Geologic Processes* (eds Valley JW, Taylor HP, Jr, O'Neil JR). Reviews of Mineralogy, **16**, 165–184.
- Sheppard SMF, Gilg HA (1996) Stable isotope geochemistry of clay minerals; the story of sloppy, sticky, lumpy and tough, Cairns-Smith (1971). *Clay Mineralogy*, **31**, 1–24. doi:10.1180/claymin.1996.031.1.01.
- Sibson RH (1996) Structural permeability of fluid-driven fault-fracture meshes. *Journal of Structural Geology*, **18**, 1031–1042.
- Smith C (1983) Thermal hydrology and heat flow of Beowawe geothermal area, Nevada. *Geophysics*, **48**, 618–626.
- Smith GI, Friedman I, Veronda G, Johnson CA (2002) Stable isotope compositions of water in the Great Basin, United States: 3. Comparison of ground waters with modern precipitation. *Journal of Geophysical Research*, **107**, 4402. doi:10.1029/2001JD000567.
- Struhsacker EM (1980) The geology of the Beowawe Geothermal System, Eureka and Lander Counties, Nevada. University of Utah Research Institute Report, ESL-37.
- Wang CY, Manga M (2010) Hydrologic responses to earthquakes—A general metric. *Geofluids*, **10**, 206–216.
- Wang CY, Wang CH, Kuo CH (2004) Temporal change in groundwater level following the 1999 ($M_w = 7.5$) Chi-Chi earthquake, Taiwan. *Geofluids*, **4**, 210–220.
- Watt JT, Glen JMG, John D, Ponce DA (2007) Three-dimensional geologic model of the northern Nevada rift and the Beowawe geothermal system, north-central Nevada. *Geosphere*, **3**, 667–682.
- Welch AH, Bright DJ, Knochenmus LA (2007) Water resources of the Basin and Range carbonate-rock aquifer system in White Pine County, Nevada, and adjacent areas in Nevada and Utah. United States Geological Survey Scientific Investigations Report, 5261, 96.
- Welhan JA, Poredai RJ, Rison W, Craig H (1988) Helium isotopes in geothermal and volcanic gases of the western United States, I. Regional variability and magmatic origin. *Journal of Volcanology and Geothermal Research*, **34**, 185–199.
- Wesnousky SG, Barron AD, Briggs RW, Caskey SJ, Kumar S, Owen L (2005) Paleoseismic transect across the northern Great Basin. *Journal of Geophysical Research*, **110**, 1–25.
- White DE (1998) The beowawe geysers, Nevada, before geothermal development. *United States Geological Survey Bulletin*, **1998**, 1–31.
- Winograd IJ, Thordarson W (1975) Hydrogeologic and hydrochemical framework, south-central Great Basin, Nevada-California, with special reference to the Nevada Test Site. United States Geological Survey Professional Paper, 712-C, 126.
- Zhang LG, Jingxiu L, Zhensheng C, Huanbo Z (1994) Experimental investigations of oxygen isotope fractionation in cassiterite and wolframite. *Bulletin of the Society of Economic Geology*, **89**, 150–157.
- Zheng YF (1999) Oxygen isotope fractionations in carbonate and sulfate minerals. *Journal of Geochemistry*, **33**, 109–126.
- Ziagos J, Blackwell D (1986) A model for the transient temperature effects of horizontal fluid flow in geothermal systems. *Journal of Volcanology and Geothermal Research*, **27**, 371–397.
- Zoback ML (1979) A geologic and geophysical investigation of the Beowawe geothermal area, north-central Nevada. *Stanford University School of Earth Sciences*, **16**, 1–79.